

Analysis of vehicle-integrated photovoltaics and vehicle-to-grid on electric vehicle battery life

Kouzelis, Antonios; Linders, Koen; Bandyopadhyay, Soumya; Mouli, Gautham Ram Chandra

DOI

[10.1016/j.jpowsour.2024.236117](https://doi.org/10.1016/j.jpowsour.2024.236117)

Publication date

2025

Document Version

Final published version

Published in

Journal of Power Sources

Citation (APA)

Kouzelis, A., Linders, K., Bandyopadhyay, S., & Mouli, G. R. C. (2025). Analysis of vehicle-integrated photovoltaics and vehicle-to-grid on electric vehicle battery life. *Journal of Power Sources*, 631, Article 236117. <https://doi.org/10.1016/j.jpowsour.2024.236117>

Important note

To cite this publication, please use the final published version (if applicable). Please check the document version above.

Copyright

Other than for strictly personal use, it is not permitted to download, forward or distribute the text or part of it, without the consent of the author(s) and/or copyright holder(s), unless the work is under an open content license such as Creative Commons.

Takedown policy

Please contact us and provide details if you believe this document breaches copyrights. We will remove access to the work immediately and investigate your claim.



Analysis of vehicle-integrated photovoltaics and vehicle-to-grid on electric vehicle battery life

Antonios Kouzelis ^a,* , Koen Linders ^a,* , Soumya Bandyopadhyay ^b,* ,
Gautham Ram Chandra Mouli ^a,*

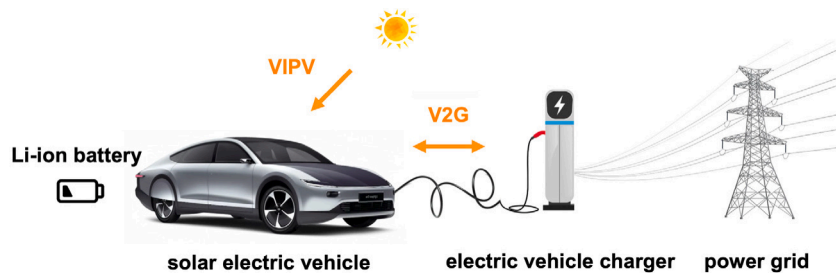
^a Delft University of Technology, Mekelweg 4, 2628CD, Delft, The Netherlands

^b Lightyear, Automotive Campus 70, 5708 JZ, Helmond, The Netherlands

HIGHLIGHTS

- Gradual VIPV charging can reduce grid charging frequency by 23%.
- Gradual VIPV charging can reduce calendar ageing by 9% in the first year.
- Cycling for V2G can reduce battery life by 12.5 years for NMC and 3.9 years for LFP.

GRAPHICAL ABSTRACT



ARTICLE INFO

Keywords:

Battery ageing
Degradation
Electric vehicles
Solar
Vehicle-integrated photovoltaics
Vehicle-to-grid
Modelling

ABSTRACT

Electric vehicles (EVs) with vehicle-integrated photovoltaics (VIPV) and vehicle-to-grid (V2G) technology can help address power grid challenges arising from the energy transition. While VIPV and V2G offer widespread benefits, their impact on EV battery life affects their economic viability. Many existing studies examining the impact of VIPV and V2G on EV battery life do not fully capture the complexity of real-world battery usage, often relying on less detailed battery data. This work models and combines detailed and validated EV battery data with validated battery ageing models to determine the impact of VIPV and V2G on EV battery life. First, a validated EV battery simulation model is used to generate realistic, per-second battery data for an EV operating in The Netherlands and Spain. Following this, VIPV power profiles, V2G day-ahead energy trading power profiles, and V2G automatic frequency restoration reserve power profiles are integrated with the battery data. Subsequently, battery datasets for different scenarios are implemented in both NMC and LFP-based semi-empirical ageing models to quantify calendar and cycling ageing capacity loss. The results show that gradual VIPV charging decreases the required annual grid charging frequency by 23% in The Netherlands and 44% in Spain, leading to lower SoC ranges, which can reduce NMC and LFP calendar ageing capacity loss by 9% in both countries. Additional cycling due to V2G day-ahead energy trading can shorten battery life by up to 12.5 years for NMC and up to 3.9 years for LFP. Moreover, the research indicates that ageing models based on tests with regular power profiles may not accurately estimate cycling ageing in power profiles with increased irregularity caused by VIPV and V2G.

* Corresponding authors.

E-mail addresses: kouzelisantionios@gmail.com (A. Kouzelis), G.R.ChandraMouli@tudelft.nl (G.R.C. Mouli).

<https://doi.org/10.1016/j.jpowsour.2024.236117>

Received 8 June 2024; Received in revised form 19 December 2024; Accepted 22 December 2024

Available online 22 January 2025

0378-7753/© 2025 The Authors. Published by Elsevier B.V. This is an open access article under the CC BY license (<http://creativecommons.org/licenses/by/4.0/>).

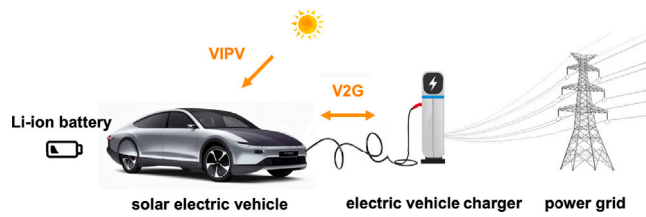


Fig. 1. Illustration of the energy flows of the Lightyear 0 charging its battery using VIPV and discharging it using V2G.

1. Introduction

Li-ion batteries are the most expensive component in electric vehicles (EVs), driving the need for battery longevity. This research examines the impact on battery life of vehicle-integrated photovoltaics (VIPV), which enables EVs to charge from solar energy, and vehicle-to-grid (V2G) technology, which allows EVs to discharge power back to the grid. Fig. 1 shows the energy flows of an EV charging its battery using VIPV and discharging it into the power grid using V2G.

1.1. VIPV and V2G

VIPV and V2G can support grid operators in overcoming power grid challenges. EVs that partially charge using VIPV are often designed to be energy-efficient, reducing grid power demand and thereby helping ease grid congestion compared to traditional EVs [1]. EVs with V2G can enable a more reliable power grid by enabling EVs to trade on energy markets and offer grid balancing services to transmission system operators (TSOs). To realise a widespread implementation of VIPV and V2G, the technologies must be cost-effective. By discharging and charging the battery, VIPV and V2G impact the EV's battery life, affecting the economic viability of these technologies [2].

1.2. Li-ion battery ageing and (semi-)empirical ageing models

Understanding Li-ion battery degradation is crucial for assessing the impact of V2G and VIPV on battery life. Battery degradation can be split into calendar ageing and cycling ageing. Calendar ageing is always present and degrades the battery during usage and resting. Cycling ageing is only present during usage and results from charging/discharging the battery. A comprehensive review of degradation mechanisms is presented in [3]. Factors such as low SoC levels (<10%), high SoC levels (>90%), low temperatures (<5 °C), high temperatures (>30 °C), high C-rates (>1 C), and deep discharge cycles, accelerate ageing [4–8]. One of the major contributors to ageing is the Solid Electrolyte Interphase (SEI) layer [9]. The SEI layer forms on the anode surface because the electrochemical potential of graphite is outside the stability window of the electrolyte, causing the electrolyte solvent and salts to react with the lithium [9]. The SEI layer contributes to calendar and cycling ageing. SEI formation is accelerated by high SoC and high temperatures [5,6,10,11]. During cycling, SEI formation can be accelerated through side reactions like particle cracking [12] and transition metal dissolution [13]. Another large ageing mechanism is Lithium plating [14], where lithium is deposited on the anode surface instead of intercalating into the anode particle. Lithium plating is accelerated at low temperatures, high charging current, and high SoC levels [4,15,16].

(Semi-)empirical ageing models curve-fit the relation of ageing stress factors onto ageing data to derive equations for estimating battery calendar and cycling ageing. These models are often used in system design and smart charging analyses due to their mathematical simplicity, providing intuitive insight into how the ageing stress factors affect ageing [4]. Despite their advantages, these models are based on specific operating conditions and cell chemistries, and are not designed to analyse highly irregular power profiles, leading to potential inaccuracies in ageing estimations.

Table 1

Literature on the impact of VIPV and V2G on battery ageing indicating the cathode chemistry, the used degradation model, and if battery temperature is included.

Study	Year	Case	Cathode	Model	Temp.
Mallon et al. [17]	2017	VIPV	LFP	[18]	–
Zhou et al. [18]	2011	V2G	LMO	[23]	–
Wang et al. [1]	2016	V2G	NMC-LMO	[24]	x
Dubarry et al. [19]	2017	V2G	NCA	Meas.	x
Uddin et al. [20]	2017	V2G	NCA	[20]	x
Steffen et al. [2]	2020	V2G	NMC	[5]	–
Schwenk et al. [22]	2023	V2G	?	?	x

1.3. Literature review

The only study identified on the impact of VIPV on EV battery life [17], examined the impact of onboard solar panels on the cycle life of an electric bus' Li-ion battery. The study suggests that as gradual solar charging reduces the required number of battery cycles, battery cycle life may extend by up to 19% if VIPV are mounted on the roof and the sides of the bus. However, the model only factors in the battery's DoD at the end of the day, neglecting the effects of minor cycles due to gradual solar charging throughout the day, as well as overlooking the battery's temperature and average SoC. Furthermore, the authors defined the battery's end of life (EoL) when cycling ageing had caused a 20% capacity loss, neglecting the contribution of calendar ageing to the battery's overall degradation.

Researchers generally agree that additional cycling for V2G services is harmful to battery life. Zhou et al. [18] modelled the cost of EV battery ageing due to V2G. The research highlights the effect of DoD on ageing cost per kWh at peak electricity rate. In addition, the study compares the cost of battery ageing to the cost of energy purchased and to the benefits of energy sales to the utility grid. The researchers, however, disregarded the thermal management of the EV's battery, posing inherent limitations to the analysis. Steffen et al. [2] researched optimal EV charging considering the effects of a financial incentive on battery ageing. The authors state that with an appropriate thermal strategy, no significant additional battery ageing should occur. Wang et al. [1] quantified EV battery ageing from driving compared to using an EV for V2G services and driving. The simulations used for the research incorporated a detailed thermal management model. The study found that if V2G were only used 20 times per year, the 10-year average capacity losses would be a maximum of 1.18% more than without the V2G services. Dubarry et al. [19] and Uddin et al. [20] studied the ageing of similar Li-ion NCA battery technologies. Dubarry et al. [19] and Uddin et al. [20] had varying findings on battery ageing due to V2G. These researchers collaborated and published a paper in 2018, clearing up how battery ageing due to V2G can be managed to extend battery lifespan using a smart control algorithm [21]. A study on the impact of V2G services on battery ageing shows that battery ageing is highly temperature-sensitive and therefore requires precise thermal models and that overlooking ageing can substantially underestimate V2G-related EV operating costs [22].

An overview of the relevant literature on the impact of VIPV and V2G on Li-ion batteries is summarised in Table 1 below.

1.4. Research contribution

This study represents an advancement in understanding the effects of VIPV and V2G on EV battery life. Building upon the limited existing research in this area, particularly on VIPV battery ageing, this work introduces a novel and comprehensive approach by integrating detailed and validated per-second EV battery data with semi-empirical ageing models, specifically to account for the irregular power profiles generated by VIPV and V2G. Unlike previous studies, which often rely on simplified models and overlook real-world conditions, this research examines a broader set of battery ageing stress factors, such as

state of charge, temperature, and charge/discharge cycles, across two geographical settings and two Li-ion battery chemistries. The novelty of this approach make it one of the most holistic analyses of in this area, leading to the following key contributions:

- Holistic Analysis of VIPV on Battery Ageing with Comprehensive Stress Factors:** This study advances the limited existing research on VIPV's impact on battery life by incorporating a wider spectrum of ageing stress factors, including time t [s], state of charge $SoC(t)$ [%], temperature $T(t)$ [°C], voltage $U(t)$ [V], current $I(t)$ [A], C -rate(t) [h^{-1}], and throughput $Q(t)$ [Ah]. Additionally, unlike previous research that only considers cycling ageing capacity loss, this study conducts a more thorough analysis by also considering calendar ageing capacity loss. This extensive approach provides a more accurate depiction of the total ageing process to improve our understanding of VIPV interactions with EV batteries.
- Comprehensive and Realistic power profile Modelling using Advanced Simulation Tools:** The integration of Lightyear's Vehicle Performance Model (VPM), Lightyear's VIPV SolarSimulator tool, and V2G modelling using mixed-integer linear programming (MILP), enables the simulation of detailed per-second EV battery power profiles. This approach improves previous methodologies by including a wide range of dynamic factors such as electric motor characteristics, regenerative braking, thermal management systems, VIPV systems, and V2G services. The enhanced detail in the modelled battery power profile improves the precision in estimating battery ageing to offer a more nuanced understanding of the impact of VIPV and V2G on EV batteries.
- Battery Ageing Model Analysis Covering Multiple Battery Chemistries and Geographical Variations:** A distinct feature of this research is the use of two semi-empirical ageing models, analysing both NMC and LFP batteries. This comprehensive approach allows for a comparative analysis of how different battery chemistries respond to identical influences of VIPV and V2G. Additionally, by considering two distinct geographical locations, Amsterdam, the Netherlands and Madrid, Spain, the study incorporates the effects of varying ambient temperatures and solar irradiance on VIPV performance and subsequent battery ageing.
- Analysis of VIPV and V2G Synergies in EV Battery Life:** The research offers novel insights into the integration of VIPV and V2G technologies with EVs. By analysing the interaction of these technologies under different operational conditions, the study contributes to a deeper understanding of their cumulative impact on battery ageing. This comprehensive analysis guides future design and implementation strategies for VIPV and V2G systems to support battery longevity.

These contributions offer a more complete and nuanced understanding of the impact of VIPV and V2G on EV battery life. The findings not only fill existing gaps in the literature but also provide actionable insights for policymakers, EV manufacturers, and researchers to support a sustainable and efficient integration of VIPV and V2G technologies in EVs.

1.5. Structure of the paper

Section 2 provides an in-depth description of the methodology used for simulating NMC and LFP Li-ion battery datasets and ageing, impacted by VIPV and V2G. Subsequently, Section 3 presents the results of the battery ageing simulations, focusing on the impact of VIPV and V2G on battery life. Finally, Section 4 gives an overview of the key findings, the potential implications of semi-empirical battery ageing models, and recommendations for future research in the field of EV battery ageing modelling.

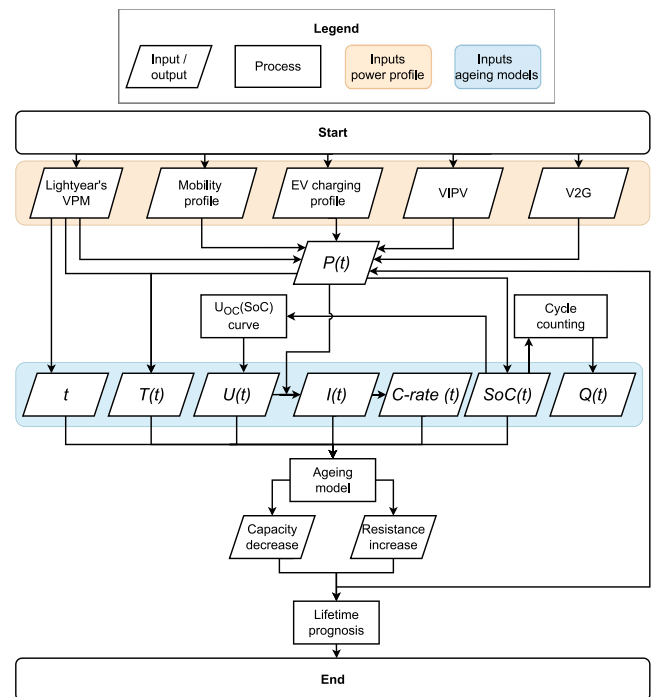


Fig. 2. Flowchart illustrating the EV battery ageing modelling methodology used in this work.

2. Modelling methodology

This section explains the methodology for modelling EV battery data, both with and without the influence of VIPV and V2G. The process involves generating and merging detailed battery power profiles to generate per-second data of the battery ageing stress factors. These battery ageing stress factors are subsequently integrated into semi-empirical battery ageing models to assess capacity decrease over time. The modelling methodology used in this work could be adapted for real-time applications by linking real-time battery ageing stress factor data to a cell-specific battery ageing model.

2.1. Simulating EV battery data

Fig. 2 shows the EV battery ageing modelling methodology. In this methodology, several inputs generate the power profile which subsequently serves as the basis for deriving battery ageing stress factors, namely $SoC(t)$ [%], $T(t)$ [°C], $U(t)$ [V], $I(t)$ [A], C -rate(t) [h^{-1}], and $Q(t)$ [Ah]. Finally, the semi-empirical battery ageing models use the battery ageing stress factors to determine the capacity decrease over time. The methodology of modelling EV battery ageing that was used in this work is detailed below.

2.1.1. Lightyear's VPM

Lightyear's VPM is an EV simulation model that simulates the Lightyear 0, a highly efficient EV with integrated solar panels developed by Lightyear in 2022 and discontinued in 2023. It was promoted to achieve a 700 km range on its 60 kWh battery, excluding additional range contributed by the solar panels during driving. The EV simulation model was developed in Simulink by capturing various EV dynamics including aerodynamics, rolling resistance, motor characteristics, converters, inverters, and thermal systems for high-voltage and low-voltage batteries. To ensure that the model is accurate and representative of real-world conditions, the VPM has been validated on subsystem level, after which the data has been fed back into the model. Lightyear's VPM was used to simulate a variety of driving cycles, generating the battery ageing stress factor data required to determine battery degradation.

2.1.2. Lightyear 0 battery cells and pack configuration

The Lightyear 0 and its VPM use TerraE INR 21700 50E NMC battery cells. These cells have a nominal capacity of 5000 mAh, a usable capacity of 4909 mAh, a maximum charging voltage 4.2 V, a nominal voltage of 3.6 V, a maximum discharge current of 15 A, and a maximum resistance of 20 mΩ. The cells could operate between $-20\text{ }^{\circ}\text{C}$ and $+60\text{ }^{\circ}\text{C}$ and weigh 70 grams each.

The battery pack consists of modules that have 34 cells in parallel and 10 in series. The battery pack contains 10 such modules in series, totalling 100 cells in series. This configuration provides a total energy storage capacity of 60,086 Wh.

2.1.3. Mobility and EV charging profile

The mobility profile of a new EV was designed based on mobility data from the Dutch Central Bureau of Statistics (CBS) and a study called *Mobility in Germany* (MiG) [25,26]. In this simulation, the EV covers 19,190 km annually, including 250 commutes, 50 leisure trips, 13 weekend trips, a 2 seasonal trips. Five standard driving cycles, including the Worldwide Harmonised Light Vehicles Test Procedure (WLTC) and Artemis cycles were alternately simulated in the VPM to create a variety of one-week power profiles.

EV charging profiles were modelled using data from ElaadNL [27]. In the simulations, the battery is consistently charged up to 90% SoC with a power of $P_{\text{charging}} = 11\text{ kW}$ and an efficiency of $\eta_{\text{charging}} = 0.95$.

2.1.4. VIPV

Lightyear's SolarSimulator tool simulates the energy generated by PV cells using weather and location data. It incorporates optical, thermal, and electrical models. Initially, the optical model calculates irradiance on the surface, followed by the thermal and electrical models which determine output power. Key variables of the electrical model that influence VIPV performance include the PV panel efficiency of 22%, panel temperature and solar irradiance. Unlike Standard Test Conditions, real conditions see higher irradiance increasing the temperature of the panels, thus reducing the power output of the VIPV system. Therefore, both panel temperature and irradiance are used as input for the thermal and electrical models. The optical model, using ray-tracing, estimates irradiance, integrating an all-weather model for sky luminance [28]. The model also considers shading from city buildings affecting the VIPV system's power output. The thermal model examines heat transfer via conduction, radiation, and convection. The electrical model employs a single-diode approach, requiring three parameters: short-circuit current (ISC), V_{OC} , and the diode ideality factor n . The model includes a series resistance R_s to better account for environmental changes, which improves the model's reliability and computational efficiency.

In Fig. 3, the top graph shows a one-week battery power and SoC profile without VIPV, and the bottom graph shows the same week with VIPV. The simulation covers regular weekday commuting and leisure trips on Wednesday evenings and the weekend. VIPV charging leads to more irregular power profiles and reduces the number of grid charging sessions by 23% in the Netherlands and 44% in Spain. The gradual VIPV charging causes the SoC to range at mid-levels for longer, which is beneficial for calendar ageing.

2.1.5. V2G

V2G power profiles were modelled using MILP, with data derived from the EPEX SPOT day-ahead (DA) market and the Dutch automatic frequency restoration reserve (aFRR) market, which are interesting V2G services for EVs in the Netherlands.

DA trading involves forecasting daily VIPV energy production to optimise the balance of EV charging and V2G discharging based on electricity prices, as outlined in Eqs. (1)–(2):

$$\text{minimise } \sum_t \epsilon_{\text{DA},t} \cdot (P_{\text{charge},t} - P_{\text{V2G},t}) \quad (1)$$

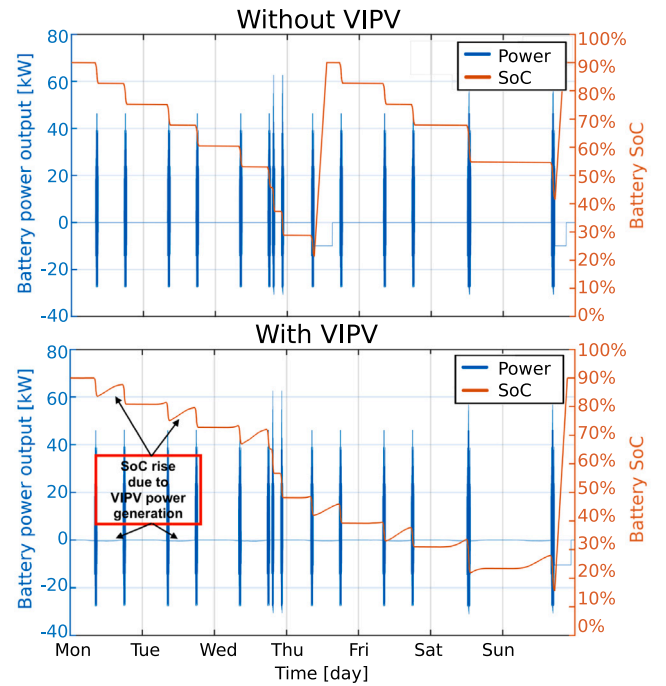


Fig. 3. Two plots showing a one-week power profile (left y-axis) and SoC profile (right y-axis), without VIPV (top graph) and with VIPV (bottom graph), illustrating the impact of VIPV on a one-week SoC profile.

$$E_{\text{stored},t} = E_{\text{start},t-1} + (P_{\text{charge},t-1} \cdot \eta_{\text{charge}} - \frac{P_{\text{V2G},t-1}}{\eta_{\text{charge}}} - P_{\text{drive},t-1}) \quad (2)$$

where:

- $\epsilon_{\text{DA},t}$ is the electricity price on the DA market in €/kWh,
- $P_{\text{charge},t}$ is the charging power from the grid in kW,
- $P_{\text{V2G},t}$ is the discharging power to the grid in kW,
- E_{stored} is the energy stored in the EV's battery in kWh,
- η_{charge} is the EV's charging efficiency,
- $P_{\text{drive},t}$ is the power used for driving the vehicle in kW.

For aFRR, EVs contribute to grid stability by adjusting their charging speed based on the grid demands of the transmission system operator, through both upward and downward regulation. The aFRR model uses bid and acceptance strategies to manage grid imbalances. Key equations for this process are shown in Eqs. (3) and (4), which represent the bids for downward and upward regulation, respectively:

$$B_{\text{down},\tau} = \max(\epsilon_{\text{aFRR},\tau}, 0) \quad (3)$$

$$B_{\text{up},\tau} = \epsilon_{\text{aFRR},\tau} \quad (4)$$

$B_{\text{down},\tau}$ ensures that bids for downward regulation are placed only when economically favourable, while $B_{\text{up},\tau}$ sets the bid for upward regulation based on the current aFRR tariff.

SoC retention limits during V2G are set at 50% and 20% for the modelled V2G scenarios to balance V2G participation with the need for sufficient EV driving range. Thereby, the SoC limits ensure that the EVs maintain battery energy capacity for emergency driving needs while maximising their grid services potential. This balancing act affects the feasibility and attractiveness of participating in V2G services, although EV battery degradation due to participation in grid services should be accounted for.

In Fig. 4, the top graph shows a battery power and SoC profile without V2G and the bottom graph shows a battery power and SoC profile including V2G day-ahead energy trading with a 50% SoC retention

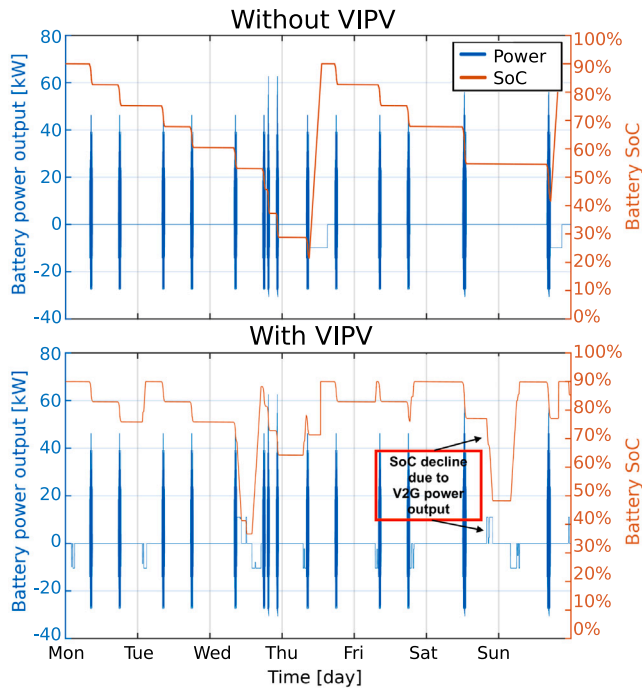


Fig. 4. Two plots showing a one-week power profile (left y-axis) and SoC profile (right y-axis), without V2G (top graph) and with V2G (bottom graph), illustrating the impact of V2G on a one-week SoC profile.

strategy.

2.1.6. $P(t)$ and $SoC(t)$

The battery power profiles modelled using Lightyear’s VPM are combined with VIPV power profiles generated by Lightyear’s VIPV SolarSimulator tool and V2G power profiles developed using MILP. Eq. (5) shows that the SoC profile is derived from the battery energy storage profile $E_{batt}(t)$ and is calculated by subtracting the integration of the power profile $P(t)$ from the initial battery capacity. In the power profile, positive values correspond to the power output required to drive the vehicle forward and to power auxiliaries, and negative values correspond to power input due to grid charging and regenerative braking.

$$E_{batt}(t) = E_{batt}(t = 0) - \int P(t) dt \quad (5)$$

Subsequently, Eq. (6) derives the SoC profile by dividing the stored battery energy capacity $E_{bat}(t)$ by the full battery capacity E_{batt}^{full} . E_{batt}^{full} equals 60 kWh at $t = 0$ and slightly decreases over time due to battery capacity degradation.

$$SoC(t) = \frac{E_{batt}(t)}{E_{batt}^{full}} \quad (6)$$

Fig. 5 shows four one-year SoC profiles, showing the impact of VIPV and V2G on cycling frequency relative to the base scenario. Fig. 5a corresponds to the base scenario, Fig. 5b to the $VIPV_{NL}$ scenario, Fig. 5c to the $V2G_{DA}^{20\% SoC}$ scenario, and Fig. 5d to the $V2G_{aFRR}^{50\% SoC}$ scenario. Compared to the base scenario, the $VIPV_{NL}$ scenario shows a reduced grid charging frequency and an increase in small variations. The $V2G_{DA}^{20\% SoC}$ and $V2G_{aFRR}^{50\% SoC}$ scenarios show a significant increase in grid charging frequency caused by additional cycling for V2G services.

2.1.7. $T(t)$

The temperature profile is modelled based on the power profile, SoC profile, and various EV characteristics determined from the VPM. The

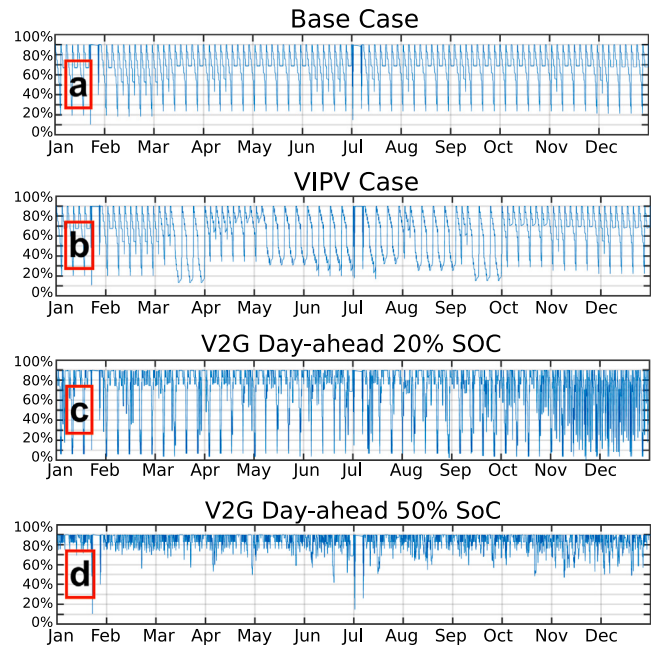


Fig. 5. Overview of the one-year SoC graphs for the base, $VIPV_{NL}$, $V2G_{DA}^{20\% SoC}$, and $V2G_{aFRR}^{50\% SoC}$ scenarios (in order from top to bottom graph), illustrating the impact of VIPV and V2G on a one-year SoC profile.

modelling of the battery temperature profile includes separate scenarios: the decrease to ambient temperature during parking, preheating to 5 °C, precooling to 25 °C, active cooling at 35 °C, the increase in temperature during driving, and the increase in temperature during charging.

Eq. (7) demonstrates that the heat transfer rate for battery cooling, preconditioning, and active cooling processes are modelled using Newton’s law of cooling.

$$\frac{dT}{dt} = -\frac{h}{c} \cdot A \cdot (T_{amb} - T_{batt}) \quad (7)$$

where h is the heat transfer coefficient, c is the battery pack’s heat capacity, A is the battery pack’s surface area, T_{amb} is the ambient temperature, and T_{batt} is the initial temperature of the battery pack. The heat transfer coefficient is assumed to be 10 W / (m² K) at the bottom side of the battery pack, and 5 W / (m² K) at the cabin side. Lightyear’s battery pack dimensions correspond to an area of 2.88 m². Lightyear’s battery cells, battery enclosure, and battery coolant, have a total heat capacity of 380 kJ/K.

Managing the battery temperature using a high-voltage air conditioning (HVAC) system demands power from the battery, for which a power penalty is incorporated in the modelled power profile until the battery reaches the desired battery temperature. The energy required to adjust the battery’s temperature to the desired operating range is calculated using Eq. (8).

$$E_{req}^{HVAC} = \frac{\Delta T \cdot c}{3,600 \cdot COP} \quad (8)$$

where E_{req}^{HVAC} is the energy required to enable the HVAC system to manage the battery’s temperature, ΔT is the temperature difference, c is the sum of the heat capacity of the battery pack components, and COP represents the coefficient of performance, which is a function of temperature. The power penalty is modelled by distributing the energy requirement E_{req}^{HVAC} evenly over the duration needed to achieve the desired battery temperature.

The battery temperatures are governed by ambient temperatures. Each morning and evening in January, the battery preheats from the ambient temperature to 5 °C. During parking, the battery cools down

to the ambient temperature according to Eq. (7). The rate of battery temperature increase during driving, consistently assumed to be 2.58 °C per hour in the temperature profile modelling, is based on VPM simulation analyses that examined the battery temperature increase over time and relative to the distance travelled, under various initial battery temperatures and ambient conditions. The rate of battery temperature increase during charging is assumed to be equal to the battery temperature increase during driving.

2.1.8. $U(t)$

The voltage profile is derived from the SoC profile and the cell-specific $U_{OC}(SoC)$ curve, which ranges from 2.8 V to 4.15 V. The average voltage of the battery cells is calculated using Eq. (9):

$$U_{cell}(t) = U_{OC}(SoC(t)) - \Delta U_{cell}(t) \quad (9)$$

where $U_{cell}(t)$ is the average voltage of the battery cells in the battery pack, $U_{OC}(SoC(t))$ is the open-circuit voltage of the battery cell, which is the difference in electrical potential between the two electrodes of a battery cell when no current is applied, and $\Delta U_{cell}(t)$ is the voltage drop over the battery cell's resistance. The voltage drop over a cell's resistance is calculated using Eq. (10):

$$\Delta U_{cell}(t) = R_{cell}(t) \cdot I_{cell}(t) \quad (10)$$

where $R_{cell}(t)$ is the resistance of the battery cell and $I_{cell}(t)$ is the average current running through the battery cell. $R_{cell}(t)$ depends on the cell's SoC and the cell's temperature.

2.1.9. $I(t)$

The current profile is derived from the power and voltage profiles. Eq. (11) shows that the average cell's current $I_{cell}(t)$ is calculated in amperes by dividing the battery pack's total power output $P_{pack}(t)$ by the cell's voltage $U_{cell}(t)$.

$$I_{cell}(t) = \frac{P_{pack}(t)}{N_{cells}^{series} \cdot U_{cell}(t)} \quad (11)$$

where N_{cells}^{series} is the number of cells in series, amounting to 100 in total, which add up to the battery pack's total operating voltage.

2.1.10. $C\text{-rate}(t)$

Eq. (12) shows that the C-rate profile is calculated by dividing the absolute of the average cell current $I_{cell}(t)$ in amperes by the nominal cell capacity I_{cell} in amperes for each second.

$$C\text{-rate}(t) = \frac{|I_{cell}(t)|}{I_{cell}} \quad (12)$$

2.1.11. $Q(t)$

The battery pack's throughput profile is calculated using Eq. (13). In this work, throughput is defined as the energy discharged by the battery. The throughput is determined for each second by dividing the current at each second by 3600.

$$Q_{pack}(t) = \frac{I_{cell}(t) \cdot N_{cells}^{parallel}}{3,600} \quad (13)$$

where $Q_{pack}(t)$ is the battery pack's total throughput and $N_{cells}^{parallel}$ is the number of cells in parallel, amounting to 34, which add up to the battery pack's total operating current.

The throughput per cycle is determined by taking the cumulative discharged capacity between the start and end of each partial discharge cycle. The start and end of each partial cycle is determined using the battery cycle counting method mentioned above.

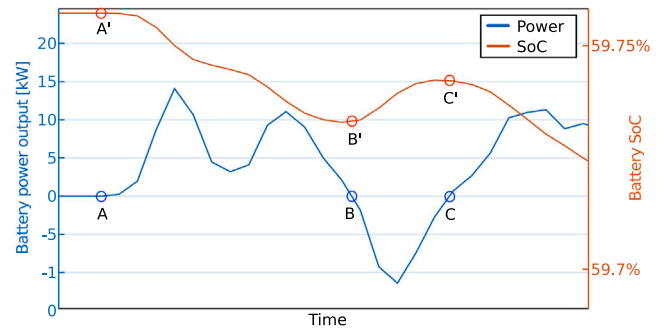


Fig. 6. Illustration of the method for counting partial battery cycles based on when the power equals 0 W.

2.2. Battery cycle counting

Battery cycle counters can be used to identify the beginning and end of each battery cycle. Two options for battery cycle counting are the rainflow cycle counting method, which is based on the battery's SoC profile [5], and the power profile cycle counting method. Rainflow cycle counting is used in engineering to determine the combined fatigue of individual stress cycles. Rainflow cycle counting is based on the assumptions that the specific sequence of different-sized cycles does not influence the fatigue, and that the impact of a cycle on fatigue is the same over the period of time over which the cycle counting is performed [29]. The power profile cycle counting method is another way to identify the beginning and end of each charge and discharge 'partial cycle'. In this approach, the start and end of a partial cycle are marked by the instances when the power profile intersects the zero mark of the y-axis ($P = 0$ W).

In this work, the power profile cycle counting method is used for cycle counting. Fig. 6 illustrates the power profile cycle counting method used in this research. The partial discharge cycle in this illustration starts at point A and ends at point B, when the power equals 0 W. The power profile's corresponding SoC profile on the right y-axis shows how the battery SoC drops from point A' to point B' during the partial discharge cycle. The partial charging cycle in the illustration starts at point B and ends at point C, when the power equals 0 W again, with the SoC profile showing the increase in battery capacity from point B' to point C'.

Eq. (14) shows that the number of full equivalent cycles n_{cycles} is determined by dividing the cell's cumulative discharged capacity $E_{discharged}^{cumulative}$ by the cell's full capacity E_{cell}^{full} .

$$n_{cycles} = \frac{E_{discharged}^{cumulative}}{E_{cell}^{full}} \quad (14)$$

2.3. Use case scenarios

The base case scenario was merged with EV battery data of VIPV and V2G to create eight distinct datasets, each analysed based on calendar and cycling battery ageing. The scenarios ranged from standard battery usage to various VIPV, V2G_{DA}, and V2G_{aFRR} configurations. The datasets were then applied to NMC and LFP-based semi-empirical ageing models. To model VIPV power generation profiles for both the Netherlands and Spain, Lightyear's SolarSimulator tool was used, incorporating irradiance and ambient temperature data derived from a typical meteorological year (TMY) dataset spanning 2010 to 2022 from the Photovoltaic Geographical Information System (PVGIS). For each month, the average temperature values were selected from this 12-year period (see Table 2).

Table 2

Use case scenarios with variations of VIPV and V2G which have been evaluated for battery ageing.

Use case scenario	Power profiles			
	Standard	VIPV	V2G _{DA}	V2G _{aFRR}
Base	V			
VIPV _{NL}	V	V		
VIPV _{ESP}	V	V		
VIPV _{NL} & V2G _{DA} ^{50% SoC}	V	V	V	
V2G _{DA} ^{50% SoC}	V		V	
V2G _{DA} ^{20% SoC}	V		V	
V2G _{aFRR} ^{50% SoC}	V			V
V2G _{aFRR} ^{20% SoC}	V			V

2.4. Semi-empirical battery ageing models

The EV battery datasets were implemented into battery ageing models sourced from the literature that showed good applicability due to clear descriptions regarding implementation compared to alternative semi-empirical battery ageing models. Specifically, the used battery ageing models include an NMC-based semi-empirical model (NMC-AM) developed by Schmalstieg et al. [5] and a semi-empirical LFP-based ageing model (LFP-AM) developed by Schimpe et al. [30].

2.4.1. NMC ageing model

NMC-AM was developed using accelerated ageing tests on 60 Sanyo UR18650E Panasonic NMC cells to address capacity decrease and resistance increase due to calendar and cycling ageing. The calendar ageing tests were conducted by taking measurements every 50 days over a period of 500 days at various SoC levels and temperatures, to establish the impact of these factors on ageing rates. The model also considered 22 cycling ageing tests under constant conditions, showing differential ageing relations based on the SoC range, thus highlighting SoC's influence on cycling ageing. Eq. (A.1)–(A.4) show the NMC-AM ageing equations that define the capacity decrease and resistance increase due to calendar ageing. Eq. (A.5)–(A.8) show the ageing equations that define the capacity decrease and resistance increase due to cycling ageing.

According to NMC-AM, calendar and cycling ageing can be superpositioned to determine total ageing. The superposition of the calendar and cycling result in two ageing equations that holistically describe capacity decrease and resistance increase, namely Eq. (15) and (16), respectively.

$$Q_1^{\text{total}} = 1 - \alpha_1^Q \cdot t^{0.75} - \beta_1^Q \cdot \sqrt{Ah} \quad (15)$$

$$R_1^{\text{total}} = 1 + \alpha_1^R \cdot t^{0.75} + \beta_1^R \cdot Ah \quad (16)$$

where t is time in days and Ah is the throughput delivered.

To assess the battery's capacity degradation, the ageing stress factors described in Section 2 are implemented using Eq. (A.7)–(16). Calendar ageing capacity loss is computed on a per-second basis and aggregated to track the total capacity loss due to calendar ageing over time. Cycling ageing capacity loss is assessed for each partial cycle, with losses from all partial cycles added sequentially according to their chronological occurrence to track the total capacity loss due to cycling ageing over time.

2.4.2. LFP ageing model

LFP-AM was developed using accelerated ageing tests on Sony US26650FTC1 LFP cells, to address capacity decrease due to calendar and cycling ageing. The calendar ageing tests were conducted over 234 days and across a range of temperatures and SoC values, focusing on time, temperature, and voltage as stress factors. Cycling ageing tests were performed at various temperatures, current levels, and C-rates.

The ageing equations that define the capacity decrease due to cycling ageing are described in Eq. (17)–(20) [30], and the reference parameters are calculated using Eq. (A.11)–(A.13). Eq. (17) shows that the capacity loss due to cycling ageing consists of three sub-equations. Eq. (18) describes cycling ageing at high temperatures, Eq. (19) describes cycling ageing at low temperatures and all SoC values, and Eq. (20) describes cycling ageing at low temperatures and SoC values above 81%, giving an extra cycling ageing weight to higher SoC cycles.

$$Q_{II}^{\text{cycling}} = Q_{\text{high T}}^{\text{cycling}} + Q_{\text{low T}}^{\text{cycling}} + Q_{\text{low T, SoC} \geq 82\%}^{\text{cycling}} \quad (17)$$

with

$$Q_{\text{high T}}^{\text{cycling}} = k_{\text{cyc, high T}} \cdot \sqrt{Ah_{\text{total}}} \quad (18)$$

$$Q_{\text{low T}}^{\text{cycling}} = k_{\text{cyc, low T}} \cdot \sqrt{Ah_{\text{charge}}} \quad (19)$$

$$Q_{\text{low T, SoC} \geq 82\%}^{\text{cycling}} = k_{\text{cyc, low T, SoC} \geq 82\%} \cdot Ah_{\text{charge}} \quad (20)$$

with the reference parameters used in these equations calculated using Eq. (19)–(A.13).

The ageing equation that determines the capacity decrease due to calendar ageing are described in Eq. (21) and (22) [30].

$$Q_{II}^{\text{calendar}} = k_{\text{cal}} \cdot \sqrt{t} \quad (21)$$

where k_{cal} is determined using

$$k_{\text{cal}} = k_{\text{cal, ref}} \cdot \exp \left[\frac{-E_{a, \text{cal}}}{R_g} \left(\frac{1}{T} - \frac{1}{T_{\text{ref}}} \right) \right] \cdot \left(\exp \left[\frac{\alpha \cdot F}{R_g} \left(\frac{U_{a, \text{ref}} - U_a(\text{SoC})}{T_{\text{ref}}} \right) \right] + k_0 \right) \quad (22)$$

where $k_{\text{cal, ref}}$ is the calendar reference stress factor which equals $3.694 \cdot 10^{-4} \text{ h}^{-0.5}$, $E_{a, \text{cal}}$ is the activation energy parameter which equals 20,592 J/mol, T_{ref} is the reference temperature which equals 298.15 K, R_g is the universal gas constant which equals 8.314 J/(mol K), F is the Faraday constant which equals 96,485 C/mol, $U_{a, \text{ref}}$ is the reference potential set at $U_a(\text{SoC} = 50\%) = 0.123 \text{ V}$, T is the battery temperature in Kelvin, and α and k_0 are fitting parameters set at 0.384 and 0.142, respectively.

LFP-AM was used in this work as this model provides insight into the anode stoichiometry on which the model is based, from which the anode open-circuit potential can be determined. Eq. (A.9) shows that the anode stoichiometry is calculated as a function of SoC through linear interpolation between 0% and 100% SoC. The anode stoichiometry given by Safari and Delacourt [31] and used by Käbitz et al. [32] to develop the model describes the relation between SoC and the degree of lithiation of the LFP anode. The LFP anode stoichiometry, used to calculate the anode open circuit voltage U_a , is derived from an NMC-motivated SoC profile due to its origin in NMC-based simulations.

The implementation of LFP-AM follows a similar implementation as NMC-AM. The calendar ageing capacity loss is determined by scaling up modelled per-second data to per-hour data, and subsequently accumulating the calendar ageing capacity loss over time. Cycling ageing capacity loss is determined per partial cycle and accumulated over charge throughput cycles and total throughput cycles according to Eq. (17) in the appendix.

3. Modelling results

Table 3 provides an overview of the results from NMC-AM and LFP-AM for each use case scenario, including one-year calendar, cycling, and total normalised capacity loss for each scenario. It details $Q_{\text{throughput}}^{\text{cell}}$, the net energy delivered by a single cell after one year, and $N_{\text{eq. full cycles}}$, and the number of full equivalent discharge cycles within a year.

The NMC-AM and LFP-AM ageing models used in this study are based on cells with 2.15 Ah and 3.00 Ah capacities, respectively, while

Table 3

One-year capacity loss of different use case scenarios, with and without VIPV or V2G, according to NMC-AM and LFP-AM.

Scenario	Ageing type	NMC-AM	LFP-AM	One-year use case characteristics			
Base	Calendar	1.05%	3.04%	$Q_{\text{throughput}}^{\text{cell}}$	342 Ah	SoC_{avg}	69%
	Cycling	2.80%	2.03%	$N_{\text{eq. full cycles}}$	70.5	DoD_{avg}	0.18%
	Total	3.85%	5.07%	$N_{\text{partial cycles}}$	70,797		
VIPV _{NL}	Calendar	0.97%	2.91%	$Q_{\text{throughput}}^{\text{cell}}$	340 Ah	SoC_{avg}	63%
	Cycling	2.81%	2.21%	$N_{\text{eq. full cycles}}$	70.1	DoD_{avg}	0.13%
	Total	3.78%	5.12%	$N_{\text{partial cycles}}$	73,642		
VIPV _{ESP} with T _{ESP}	Calendar	1.26%	3.02%	$Q_{\text{throughput}}^{\text{cell}}$	339 Ah	SoC_{avg}	58%
	Cycling	2.86%	2.07%	$N_{\text{eq. full cycles}}$	69.9	DoD_{avg}	0.14%
	Total	4.12%	5.09%	$N_{\text{partial cycles}}$	74,098		
VIPV _{NL} & V2G _{DA} ^{50% SoC}	Calendar	1.14%	3.36%	$Q_{\text{throughput}}^{\text{cell}}$	606 Ah	SoC_{avg}	76%
	Cycling	5.46%	2.40%	$N_{\text{eq. full cycles}}$	125	DoD_{avg}	0.30%
	Total	6.60%	5.76%	$N_{\text{partial cycles}}$	71,686		
V2G _{DA} ^{50% SoC}	Calendar	1.14%	3.36%	$Q_{\text{throughput}}^{\text{cell}}$	607 Ah	SoC_{avg}	76%
	Cycling	5.48%	2.40%	$N_{\text{eq. full cycles}}$	125	DoD_{avg}	0.31%
	Total	6.62%	5.76%	$N_{\text{partial cycles}}$	71,695		
V2G _{DA} ^{20% SoC}	Calendar	1.08%	3.19%	$Q_{\text{throughput}}^{\text{cell}}$	772 Ah	SoC_{avg}	71%
	Cycling	8.78%	2.94%	$N_{\text{eq. full cycles}}$	159	DoD_{avg}	0.36%
	Total	9.86%	6.13%	$N_{\text{partial cycles}}$	71,529		
V2G _{aFRR} ^{50% SoC}	Calendar	1.23%	3.64%	$Q_{\text{throughput}}^{\text{cell}}$	459 Ah	SoC_{avg}	84%
	Cycling	4.83%	1.78%	$N_{\text{eq. full cycles}}$	95	DoD_{avg}	0.24%
	Total	6.06%	5.42%	$N_{\text{partial cycles}}$	72,459		
V2G _{aFRR} ^{20% SoC}	Calendar	1.22%	3.63%	$Q_{\text{throughput}}^{\text{cell}}$	477 Ah	SoC_{avg}	83%
	Cycling	4.80%	1.83%	$N_{\text{eq. full cycles}}$	98	DoD_{avg}	0.25%
	Total	6.02%	5.46%	$N_{\text{partial cycles}}$	72,368		

the Lightyear vehicle's battery cells have a capacity of 4.85 Ah. To account for this, one approach would have been to scale the throughput in our vehicle model to match the battery ageing models. While this would have provided a more precise match for throughput-induced ageing, it would have required introducing a scaling factor into the original ageing equations without adjusting other battery cell parameters, such as the SoC profile and temperature dynamics, which also significantly impact battery ageing. To avoid altering the equations and to ensure consistency, we chose to use the throughput of the Lightyear vehicle's battery directly, despite the size difference. This simplified the study and preserved the integrity of the ageing models, while still allowing for reliable comparison of relative degradation trends across different scenarios within each battery chemistry. Consequently, while absolute degradation values should be interpreted with caution, the relative trends provide meaningful insights into the comparative impacts of VIPV and V2G on NMC and LFP batteries.

Table 3 details $N_{\text{partial cycles}}$, the number of partial cycles, SoC_{avg} , the average state of charge (SoC) over the year, and DoD_{avg} , the average cycle depth of the partial cycles throughout the year, and EoL , the year when the battery retains 80% of its initial capacity. The time period and temperature profiles are identical across all scenarios. It is important to recognise that the loss of lithium inventory due to SEI formation is more significant during the first few hundred cycles, after which the reaction rate decelerates [33]. Consequently, battery ageing in the first year might be more prominent compared to the subsequent years.

For illustration, Fig. 7 shows the one-year SoC, temperature and Q_{loss} profiles for the base scenario. The temperature spikes in January and July correspond to long-distance drives of 1876 km in January and 2696 km in July, representing seasonal holiday trips. The seasonal effect of temperature causes the wavy capacity loss pattern over the year, as differences in temperature impact battery ageing [9]. A comparison of degradation between the base case, VIPV case, and V2G_{DA}^{50%} is shown in Fig. 9.

Impact of VIPV on calendar ageing

As VIPV gradually charges the battery, it reduces the required grid charging frequency, causing the average annual SoC to range 9% lower in the Netherlands and 16% lower in Spain. Lower SoC is beneficial for calendar ageing as it decelerates the growth of the SEI layer. NMC-AM suggests that VIPV can reduce one-year calendar ageing capacity

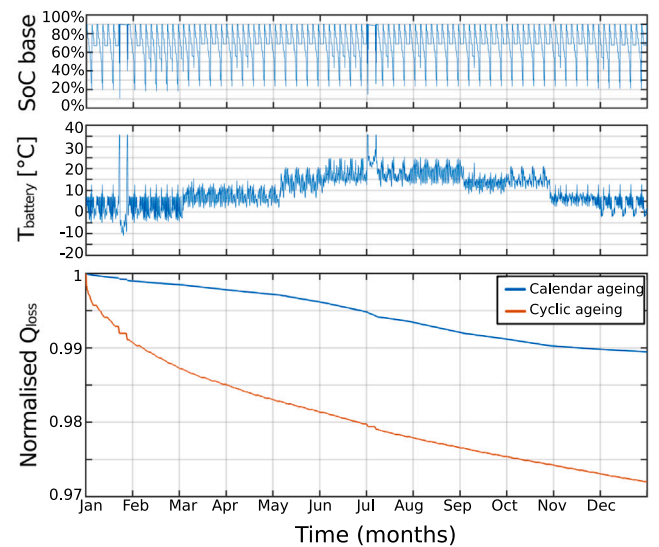


Fig. 7. Base scenario: one-year SoC, temperature and Q_{loss} profiles for an NMC battery determined using NMC-AM.

loss by 8% in the Netherlands and by 9% in Spain, suggesting that policymakers should incentivise the integration of VIPV in EVs. LFP-AM suggests that VIPV can reduce one-year calendar ageing capacity loss by 4% in the Netherlands and by 10% in Spain. This difference between the two countries is due to the increased solar irradiance in Spain, which increases VIPV's charging capacity, further decreasing the need for grid charging. Consequently, the average SoC remains at mid-levels for longer in the EV in Spain compared to the Netherlands.

Impact of VIPV on cycling ageing

Results show that cycling ageing reduces the average cycle depth by 22% in the Netherlands and 28% in Spain. Fig. 8a illustrates the cycle depths in the base scenario and Fig. 8b in the VIPV_{NL} scenario. A decrease in cycle depth is beneficial for battery cycling life [5,7,34,35]. Moreover, VIPV decreased the battery's annual throughput by 26 kWh,

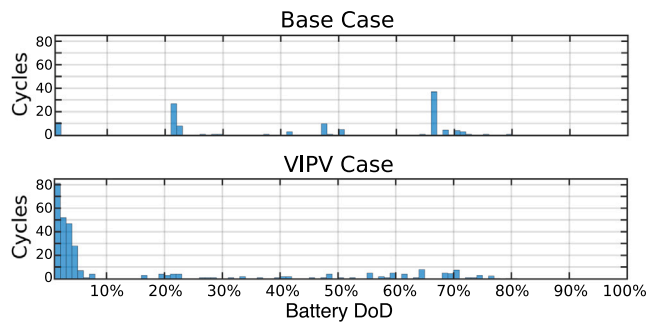


Fig. 8. Two graphs illustrating the difference in the number of cycles per cycle depth according to Matlab's rainflow cycling counting algorithm for the base scenario (top graph) and the VIPV_{NL} scenario (bottom graph).

which is beneficial for battery cycle life. In contrast, results from both ageing models suggest an increase in cycling ageing in the VIPV_{NL} scenario, which is due to the frequent transitions between charging and discharging, causing the power profile to cross the zero-watt line more often. This frequent crossing leads to an increased count of partial cycles. Despite these partial cycles being shallow and theoretically less harmful to battery ageing, the ageing models misinterpret the high frequency of these cycles as an indicator of increased cycling stress. This misinterpretation could lead to the prediction of accelerated ageing. However, the actual impact of these shallower, more frequent cycles is likely less detrimental than deeper, more intensive cycles. The reduced depth of the battery cycles should, in theory, contribute positively to battery longevity by minimising both the chemical and mechanical stresses associated with deeper discharge cycles.

Impact of V2G on calendar ageing

NMC-AM suggests that in the modelled scenario, V2G aFRR can increase one-year calendar ageing capacity loss by up to 17% due to a 22% increase in SoC. NMC-AM suggests that if the EV allows V2G services to discharge the battery to a lower battery capacity retention limit during V2G, SoC can be reduced, which reduces calendar ageing. In case the capacity retention limit during V2G is 20% SoC, NMC-AM suggests that calendar ageing can have a relative reduction of 5% compared to a 50% SoC retention limit. By implementing a controlled V2G strategy that lowers the average SoC, V2G can reduce calendar ageing.

LFP-AM suggests that V2G aFRR can increase one-year calendar ageing capacity loss by up to 16% due to a 22% increase in SoC. As for NMC-AM, increased average SoC due to V2G increased calendar ageing. Thus, V2G could lower calendar ageing by regulating the battery's SoC. In case the capacity retention limit during V2G is 20% SoC, LFP-AM suggests that calendar ageing can have a relative reduction of 5% compared to a 50% SoC retention limit due to deeper discharge cycles causing a decrease in SoC.

Impact of V2G on cycling ageing

NMC-AM suggests that V2G day-ahead energy trading with a 20% SoC retention limit during V2G can increase one-year cycling ageing by up to 214% compared to the base scenario, which would shorten battery life by up to 12.5 years. This large increase in cycling ageing is due to a 126% increase in throughput.

LFP-AM suggests that V2G day-ahead energy trading with a 20% SoC retention limit during V2G can increase one-year cycling ageing capacity loss by 45%, which could shorten battery life by 3.9 years. The increase in cycling ageing is due to a 126% increase in throughput, which causes, among other things, further growth of the SEI layer and lithium plating. It seems that V2G caused battery life to shorten significantly less in LFP-AM compared to NMC-AM. Although this phenomenon is often observed in V2G degradation studies [36–38], the comparison is hard to make in this study because the LFP-AM and NMC-AM are modelled with different cell capacities.

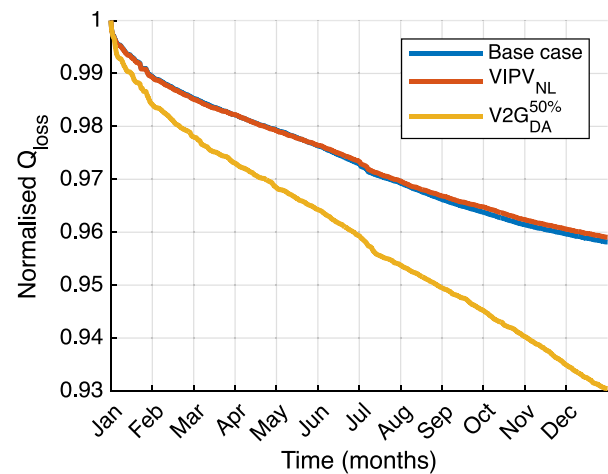


Fig. 9. Comparison between three scenarios showing the differences in degradation speed. VIPV_{NL} shows the least degradation followed by the Base case. The V2G case with Day-ahead optimisation shows the worst degradation.

4. Conclusion

EVs with VIPV and V2G technology can support in mitigating power grid challenges arising from the energy transition. While VIPV and V2G can provide widespread benefits, their impact on EV battery life is a crucial factor in their economic feasibility. Current studies on the impact of VIPV and V2G on battery life often use simplistic battery data and do not use validated battery ageing models. This paper explores the impact of VIPV and V2G on the lifetime of NMC and LFP batteries, using detailed battery power profiles and validated semi-empirical battery ageing models. Key contributions of this study are the holistic analysis of VIPV's impact on battery life with comprehensive stress factors, the use of advanced simulation tools for creating detailed EV battery power profiles, a comparative analysis of battery ageing across two chemistries and two geographical locations, and insights into the synergies between VIPV and V2G technologies.

The findings reveal that VIPV decreases the need for grid charging, leading to a lower average SoC, and reducing calendar ageing capacity loss. Specifically, VIPV can reduce NMC calendar ageing capacity loss by 9% in the Netherlands and 8% in Spain, and VIPV can reduce LFP calendar ageing capacity loss by 6% in the Netherlands and by 9% in Spain. In contrast, the simulation results indicate that V2G can increase battery cycling ageing, particularly when deployed for DA energy trading and aFRR. In this work, cycling ageing increased more significantly during DA due to higher V2G demands, leading to an accelerated capacity loss compared to the simulated aFRR applications. Additionally, calendar ageing in V2G scenarios was found to be heavily influenced by the increased SoC levels necessary for providing reliable grid support, which illustrates the trade-off between grid benefits and battery longevity.

These insights are useful for policymakers and EV manufacturers to incentivise VIPV integration and account for accelerated battery ageing caused by V2G applications. Despite VIPV reducing average cycle depth and annual throughput, the ageing models estimated increased cycling ageing capacity loss. Ongoing research should focus on refining (semi-)empirical ageing models by clarifying battery cycle definitions and battery ageing simulation methodologies. To more accurately estimate capacity loss due to cycling ageing of EV batteries that experience highly irregular power profiles, it is recommended to develop ageing models based on highly irregular power profiles, apply machine learning-based ageing models, or conduct extensive empirical cycling ageing tests.

CRedit authorship contribution statement

Antonios Kouzelis: Writing – review & editing, Writing – original draft, Visualization, Validation, Software, Resources, Project administration, Methodology, Investigation, Formal analysis, Data curation, Conceptualization. **Koen Linders:** Writing – review & editing. **Soumya Bandyopadhyay:** Writing – review & editing, Supervision, Conceptualization. **Gautham Ram Chandra Mouli:** Writing – review & editing, Validation, Supervision, Conceptualization.

Declaration of competing interest

The authors declare the following financial interests/personal relationships which may be considered as potential competing interests: Antonios Kouzelis reports financial support was provided by Lightyear. Antonios Kouzelis reports a relationship with Lightyear that includes: employment. I was a graduate research intern at Lightyear at the time. If there are other authors, they declare that they have no known competing financial interests or personal relationships that could have appeared to influence the work reported in this paper.

Appendix

NMC-AM

To develop NMC-AM, researchers from RWTH Aachen used accelerated ageing tests to design an ageing model that addresses capacity decrease and resistance increase due to calendar and cycling ageing [5]. The ageing tests were performed using 60 Sanyo UR18650E round Panasonic NMC cells (1:1:1), which have a nominal capacity of 2.15 Ah, a maximum C-rate of 3C and a specific energy of 162 Wh/kg. The Sanyo UR18650E cell is a high energy and high power battery cell ideal for e-bikes, smaller electrical appliances, and robotics.

$$Q_1^{\text{calendar}} = 1 - \alpha_1^Q \cdot t^{0.75} \quad (\text{A.1})$$

$$R_1^{\text{calendar}} = 1 + \alpha_1^R \cdot t^{0.75} \quad (\text{A.2})$$

with

$$\alpha_1^Q = (7.543 \cdot V - 23.75) \cdot 10^6 \cdot \exp\left(-\frac{6,976}{T}\right) \quad (\text{A.3})$$

$$\alpha_1^R = (5.270 \cdot V - 16.32) \cdot 10^5 \cdot \exp\left(-\frac{5,986}{T}\right) \quad (\text{A.4})$$

where Q_1^{calendar} is the battery's normalised storage capacity, R_1^{calendar} is the battery's normalised resistance, t is time in days, T is the absolute temperature of the battery in Kelvin, and V is the voltage of the battery cell. The $t^{0.75}$ term indicates that calendar-led ageing follows an exponential decay over time, which is in line with the slowing growth of the SEI layer [4]. Thus, considered calendar ageing stress factors are time, temperature, and voltage.

$$Q_1^{\text{cycling}} = 1 - \beta_1^Q \cdot \sqrt{Ah} \quad (\text{A.5})$$

$$R_1^{\text{cycling}} = 1 + \beta_1^R \cdot Ah \quad (\text{A.6})$$

with

$$\beta_1^Q = 7.348 \cdot 10^{-3} \cdot (\infty V - 3.667)^2 + 7.600 \cdot 10^{-4} + 4.081 \cdot 10^{-3} \cdot \Delta DoD \quad (\text{A.7})$$

$$\beta_1^R = 2.153 \cdot 10^{-4} \cdot (\infty V - 3.725)^2 - 1.521 \cdot 10^{-5} + 2.798 \cdot 10^{-4} \cdot \Delta DoD \quad (\text{A.8})$$

where ∞V describes the dependency on the root mean square voltage of the cycle and ΔDoD describes the cycle depth. The \sqrt{Ah} term of Eq. (A.5) indicates that cycling ageing capacity loss decreases with throughput or number of cycles. The \sqrt{Ah} term of Eq. (A.6) indicates

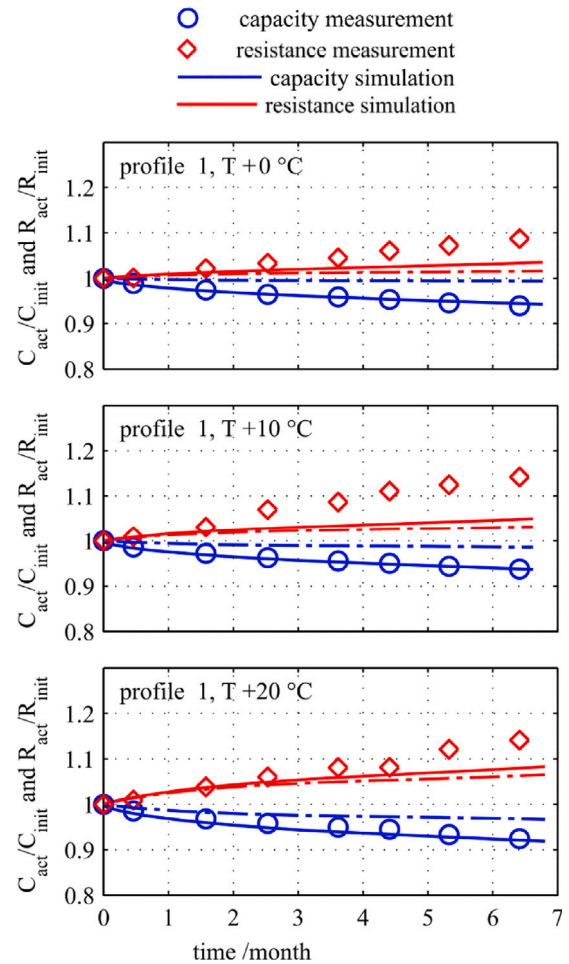


Fig. A.10. Measured ageing data (circles) and ageing simulation results (lines) by Schmalstieg et al. [5]. The dashed lines show the calendar degradation part of the cumulative degradation.

that cycling ageing resistance increases linearly with the number of cycles. Thus, considered cycling ageing stress factors are voltage, DoD, and throughput. Eq. (A.7) and (A.7) show that the capacity loss follows an exponential decay over time, which is considered through linearisation of the ageing equations over time. Note that only the capacity loss ageing equations are used in this work.

Schmalstieg et al. [5] assumed that there is little to no temperature dependency on cycling ageing, which the researchers validated using verification tests with irregular power profiles.

The validation of NMC-AM involved simulating the validation tests conducted by the authors and comparing the modelled results with their measurements. The ageing modelling results of the reproduced power profiles were compared with the measured and modelled ageing results by Schmalstieg et al. [5] to determine the accuracy of the implementation of NMC-AM. The modelled ageing results imitated the measured ageing results, showing a maximum deviation of 0.2% in ageing after six months (see Fig. A.10).

LFP-AM

To develop LFP-AM, researchers performed accelerated ageing tests over a period of 234 days to analyse the capacity decrease due to calendar and cycling ageing [30]. The ageing tests were performed on commercial cylindrical 26650-format Sony US26650FTC1 LFP cells, which have a nominal capacity of 3.0 Ah, a nominal voltage of 3.2 V,

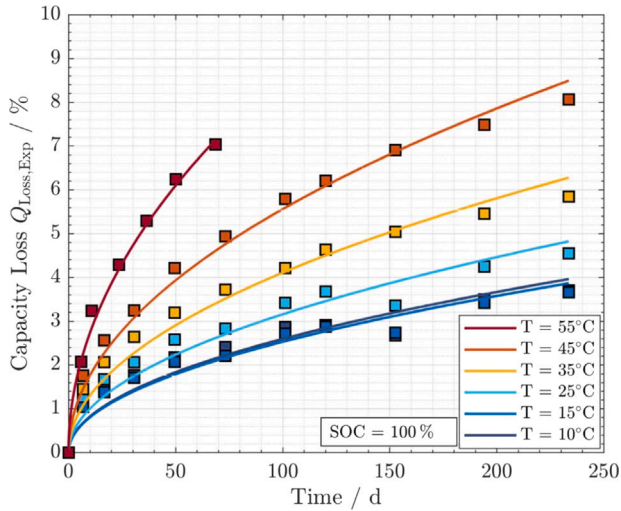


Fig. A.11. Capacity loss for the calendar ageing experiments by Schimpe et al. [30]. The squares represent experimental data and the curves represent simulations by the authors.

and are designed for stationary applications.

$$x_a(\text{SoC}) = x_a(\text{SoC} = 0\%) + \text{SoC} \cdot [x_a(\text{SoC} = 100\%) - x_a(\text{SoC} = 0\%)] \quad (\text{A.9})$$

where the degree of lithiation at 0% SoC and 100% SoC is derived by fitting the half-cell open circuit potentials of both electrodes (Anode Li-C and cathode LiFePO₄) to full-cell open circuit potential data.

Eq. (A.10) shows that the anode stoichiometry is used to determine the open circuit potential of the anode.

$$U_a(x_a) = 0.6379 + 0.5416 \cdot \exp(-305.5309 \cdot x_a) + 0.044 \cdot \tanh\left(\frac{-x_a - 0.1958}{0.1088}\right) - 0.1978 \cdot \tanh\left(\frac{x_a - 1.0571}{0.0854}\right) - 0.6875 \cdot \tanh\left(\frac{x_a + 0.0117}{0.0529}\right) - 0.0175 \cdot \tanh\left(\frac{x_a - 0.5692}{0.0875}\right) \quad (\text{A.10})$$

where U_a is the anode open circuit potential, and x_a is the degree of lithiation, taken from Safari and Delacourt [31].

In this ageing model, a distinction is made between cycling ageing effects that occur at low and high temperatures. The high-temperature cycling ageing mechanism is assumed to occur both during charging and discharging and thus independently of the current direction. In contrast, the low-temperature induced cycling ageing mechanism is assumed to occur only during charging. The researchers therefore distinguish charge throughput and total throughput defined as the sum of charge and discharge throughput. The reference parameters of the ageing equations that define the capacity decrease due to cycling ageing (Eq. (17)–(20) [30]), are calculated using Eq. (A.11)–(A.13).

$$k_{\text{cyc, high T}} = k_{\text{cyc, high T, ref}} \cdot \exp\left[\frac{-E_{a, \text{cyc, high T}}}{R_g} \left(\frac{1}{T} - \frac{1}{T_{\text{ref}}}\right)\right] \quad (\text{A.11})$$

$$k_{\text{cyc, low T}} = k_{\text{cyc, low T, ref}} \cdot \exp\left[\frac{-E_{a, \text{cyc, low T}}}{R_g} \left(\frac{1}{T} - \frac{1}{T_{\text{ref}}}\right)\right] \quad (\text{A.12})$$

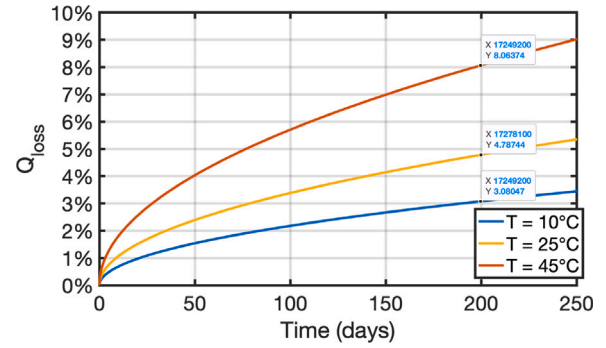


Fig. A.12. Modelled capacity loss for battery temperatures at 10 °C, 25 °C, and 45 °C and a constant 100% SoC.

$$k_{\text{cyc, low T, SoC} \geq 82\%} = k_{\text{cyc, low T, SoC} \geq 82\%, \text{ref}} \cdot \exp\left[\frac{-E_{a, \text{cyc, low T, SoC} \geq 82\%}}{R_g} \left(\frac{1}{T} - \frac{1}{T_{\text{ref}}}\right)\right] \cdot \exp\left[\beta_{\text{cyc, low T, SoC} \geq 82\%} \cdot \frac{I_{\text{charge}} - I_{\text{charge, ref}}}{C_0}\right] \cdot \left(\frac{\text{sgn}(\text{SoC} - \text{SoC}_{\text{ref}}) + 1}{2}\right) \quad (\text{A.13})$$

where k_{ref} are reference parameters set at $T_{\text{ref}} = 298.15$ K, with values $k_{\text{cyc, high T, ref}} = 1.456 \cdot 10^{-4} \cdot \text{Ah}^{-0.5}$, $k_{\text{cyc, low T, ref}} = 4.009 \cdot 10^{-4} \cdot \text{Ah}^{-0.5}$, and $k_{\text{cyc, low T, SoC} \geq 82\%, \text{ref}} = 2.031 \cdot 10^{-6} \cdot \text{Ah}^{-1}$. The temperature dependence is implemented through the Arrhenius equation where $E_{a, \text{cyc, high T}} = 32,699$ J/mol, $E_{a, \text{cyc, low T}} = 55,546$ J/mol, and $E_{a, \text{cyc, low T, SoC} \geq 82\%} = 2.3 \cdot 10^5$ J/mol. Furthermore, $I_{\text{charge, ref}} = 3$ A, $\beta_{\text{cyc, low T, SoC} \geq 82\%} = 7.8$ h, and $\text{SoC}_{\text{ref}} = 82\%$. Due to its sign function (sgn), Eq. (A.12) is only included when the SoC exceeds 82%.

To validate the implementation of the ageing model, the capacity loss measured during the ageing experiments performed to develop the ageing model, is compared with the capacity loss modelled for the base scenario, under identical temperature and SoC conditions. Fig. A.11 shows the measured capacity loss during calendar ageing tests by Schimpe et al. [30]. The authors performed these calendar ageing tests to determine the influence of temperatures ranging from 10 °C to 55 °C, at a constant 100% SoC, corresponding to 3.42 V. Fig. A.12 shows the modelled capacity loss for calendar ageing for two battery temperatures and at a constant SoC level. The figure shows that The 200-day measured capacity loss at battery temperatures of 10 °C, 25 °C, and 45 °C were 3.6%, 4.5%, and 7.9%, respectively. Fig. A.12 shows that the 200-day modelled capacity loss at battery temperatures of 10 °C, 25 °C, and 45 °C were 3.1%, 4.8%, and 8.1%, respectively. Comparing the capacity loss curves from Figs. A.11 and A.12 at the same battery temperatures, the modelled results closely follow the measured calendar ageing capacity loss results.

Data availability

Data will be made available on request.

References

- [1] D. Wang, J. Coignard, T. Zeng, C. Zhang, S. Saxena, Quantifying electric vehicle battery degradation from driving vs. vehicle-to-grid services, *J. Power Sources* (ISSN: 0378-7753) 332 (2016) 193–203, <http://dx.doi.org/10.1016/J.JPOWSOUR.2016.09.116>.
- [2] T. Steffen, A. Fly, W. Mitchell, Optimal electric vehicle charging considering the effects of a financial incentive on battery ageing, *Energies* (ISSN: 19961073) 13 (2020) <http://dx.doi.org/10.3390/EN13184742>, [Online]. Available: https://www.researchgate.net/publication/344858550_Optimal_Electric_Vehicle_Charging_Considering_the_Effects_of_a_Financial_Incentive_on_Battery_Ageing.

- [3] J.S. Edge, et al., Lithium ion battery degradation: what you need to know, *Phys. Chem. Chem. Phys.* 23 (14) (2021) 8200–8221, <http://dx.doi.org/10.1039/D1CP00359C>, [Online]. Available: <https://pubs.rsc.org/en/content/articlelanding/2021/cp/d1cp00359c>.
- [4] W. Vermeer, G.R.C. Mouli, P. Bauer, A comprehensive review on the characteristics and modelling of lithium-ion battery ageing, *IEEE Trans. Transp. Electr.* (ISSN: 23327782) (2022) <http://dx.doi.org/10.1109/TTE.2021.3138357>.
- [5] J. Schmalstieg, et al., Calendar and cycle life study of Li(NiMnCo)O₂-based 18650 lithium-ion batteries, *J. Power Sources* (ISSN: 03787753) 248 (2014) 839–851, <http://dx.doi.org/10.1016/j.jpowsour.2013.09.143>.
- [6] J. Vetter, et al., Ageing mechanisms in lithium-ion batteries, *J. Power Sources* (ISSN: 03787753) 147 (2005) 269–281, <http://dx.doi.org/10.1016/j.jpowsour.2005.01.006>.
- [7] J. de Hoog, et al., Combined cycling and calendar capacity fade modeling of a Nickel-Manganese-Cobalt Oxide Cell with real-life profile validation, *Appl. Energy* (ISSN: 0306-2619) 200 (2017) 47–61, <http://dx.doi.org/10.1016/j.apenergy.2017.05.018>, [Online]. Available: <https://www.sciencedirect.com/science/article/pii/S0306261917305251>.
- [8] M. Nie, D. Chalasani, D.P. Abraham, Y. Chen, A. Bose, B.L. Lucht, The degradation behavior of LiFePO₄/C batteries during long-term calendar aging, *J. Phys. Chem. C* 117 (3) (2013) 1257–1267, <http://dx.doi.org/10.1021/jp3118055>.
- [9] S.J. An, J. Li, C. Daniel, D. Mohanty, S. Nagpure, D.L. Wood, The state of understanding of the lithium-ion-battery graphite solid electrolyte interphase (SEI) and its relationship to formation cycling, *Carbon* (ISSN: 0008-6223) 105 (2016) 52–76, <http://dx.doi.org/10.1016/j.carbon.2016.04.008>, [Online]. Available: <https://www.sciencedirect.com/science/article/pii/S0008622316302676>.
- [10] X. Jin, et al., Comparison of Li-ion battery degradation models for system design and control algorithm development, *Proc. Am. Control. Conf.* (ISSN: 07431619) (2017) 74–79, <http://dx.doi.org/10.23919/ACC.2017.7962933>,
- [11] E. Redondo-Iglesias, P. Venet, S. Pelissier, Calendar and cycling ageing combination of batteries in electric vehicles, *Microelectron. Reliab.* (ISSN: 0026-2714) 88–90 (2018) 1212–1215, <http://dx.doi.org/10.1016/J.MICROREL.2018.06.113>.
- [12] W. Ai, B. Wu, E. Martínez-Pañeda, A coupled phase field formulation for modelling fatigue cracking in lithium-ion battery electrode particles, *J. Power Sources* (ISSN: 0378-7753) 544 (2022) 231805, <http://dx.doi.org/10.1016/j.jpowsour.2022.231805>.
- [13] J.A. Gilbert, I.A. Shkrob, D.P. Abraham, Transition metal dissolution, ion migration, electrocatalytic reduction and capacity loss in lithium-ion full cells, *J. Electrochem. Soc.* (ISSN: 1945-7111) 164 (2) (2017) A389, <http://dx.doi.org/10.1149/2.1111702jes>.
- [14] X. Lin, K. Khosravinia, X. Hu, J. Li, W. Lu, Lithium plating mechanism, detection, and mitigation in lithium-ion batteries, *Prog. Energy Combust. Sci.* (ISSN: 0360-1285) 87 (2021) 100953, <http://dx.doi.org/10.1016/j.pecs.2021.100953>.
- [15] C.R. Birkel, M.R. Roberts, E. McTurk, P.G. Bruce, D.A. Howey, Degradation diagnostics for lithium ion cells, *J. Power Sources* (ISSN: 0378-7753) 341 (2017) 373–386, <http://dx.doi.org/10.1016/J.JPOWSOUR.2016.12.011>.
- [16] L. Kong, M. Pecht, Lithium-ion Battery Technology - What is the Energy Density of a Lithium-Ion Battery? Center for Advanced Life Cycle Engineering (CALCE) Battery Research Group at the University of Maryland, 2020, [Online]. Available: <https://www.batterypoweronline.com/news/a-look-inside-your-battery-watching-the-dendrites-grow/>.
- [17] K.R. Mallon, F. Assadian, B. Fu, Analysis of on-board photovoltaics for a battery electric bus and their impact on battery lifespan, *Energies* (ISSN: 19961073) 10 (2017) <http://dx.doi.org/10.3390/en10070943>.
- [18] C. Zhou, K. Qian, M. Allan, W. Zhou, Modeling of the cost of EV battery wear due to V2G application in power systems, *IEEE Trans. Energy Convers.* (2011) [Online]. Available: <https://ieeexplore-ieee.org.tudelft.idm.oclc.org/stamp/stamp.jsp?tp=&number=5958591>.
- [19] M. Dubarry, A. Devie, K. Mckenzie, Durability and reliability of electric vehicle batteries under electric utility grid operations: Bidirectional charging impact analysis, *J. Power Sources* (2017) <http://dx.doi.org/10.1016/j.jpowsour.2017.05.015>.
- [20] K. Uddin, T. Jackson, W.D. Widanage, G. Chouchelamane, P.A. Jennings, J. Marco, On the possibility of extending the lifetime of lithium-ion batteries through optimal V2G facilitated by an integrated vehicle and smart-grid system, *Energy* (ISSN: 0360-5442) 133 (2017) 710–722, <http://dx.doi.org/10.1016/J.ENERGY.2017.04.116>.
- [21] K. Uddin, M. Dubarry, M.B. Glick, The viability of vehicle-to-grid operations from a battery technology and policy perspective, *Elsevier Energy Policy* (2018) <http://dx.doi.org/10.1016/j.enpol.2017.11.015>.
- [22] K. Schwenk, S. Meisenbacher, B. Briegel, T. Harr, V. Hagenmeyer, R. Mikut, Integrating battery aging in the optimization for bidirectional charging of electric vehicles, *IEEE J. Electrochem. Soc.* (ISSN: 2168-2364) (2023) A616–A628, <http://dx.doi.org/10.1109/JBAS.2023.9493733>, [Online]. Available: <https://ieeexplore.ieee.org/document/9493733>.
- [23] P. Rong, M. Pedram, An analytical model for predicting the remaining battery capacity of lithium-ion batteries, *IEEE Trans. Very Large Scale Integr. (VLSI) Syst.* (ISSN: 1557-9999) 14 (5) (2006) 441–451, <http://dx.doi.org/10.1109/TVLSI.2006.876094>, [Online]. Available: <https://ieeexplore.ieee.org/document/1650223>.
- [24] J. Wang, et al., Degradation of lithium ion batteries employing graphite negatives and nickel-cobalt-manganese oxide + spinel manganese oxide positives: part 1, aging mechanisms and life estimation, *J. Power Sources* (ISSN: 0378-7753) 269 (2014) 937–948, <http://dx.doi.org/10.1016/j.jpowsour.2014.07.030>, [Online]. Available: <https://www.sciencedirect.com/science/article/pii/S037877531401074X>.
- [25] CBS, Hoeveel rijden personenauto's? 2021, [Online]. Available: <https://www.cbs.nl/nl-nl/visualisaties/verkeer-en-vervoer/verkeer/verkeersprestaties-personeenauto's>.
- [26] German Federal Ministry for Digital and Transport, Mobility in Germany study, 2017, [Online]. Available: <https://www.bmvi.de/EN/Services/Statistics/Mobility-in-Germany/mobility-in-germany.html>.
- [27] ElaadNL, Open datasets for electric mobility research, 2020, [Online]. Available: https://platform.elaad.io/analyses/ElaadNL_opendata.php.
- [28] R. Perez, R. Seals, J. Michalsky, All-weather model for sky luminance distribution-preliminary configuration and validation, *Sol. Energy* (1993).
- [29] Y.-L. Lee, T. Tjhung, Rainflow cycle counting techniques, *Met. Fatigue Anal. Handb.* (2012) 89–114, <http://dx.doi.org/10.1016/B978-0-12-385204-5.00003-3>,
- [30] M. Schimpe, M.E. von Kuepach, M. Naumann, H.C. Hesse, K. Smith, A. Jossen, Comprehensive modeling of temperature-dependent degradation mechanisms in lithium iron phosphate batteries, *J. Electrochem. Soc.* (ISSN: 0013-4651) 165 (2018) A181–A193, <http://dx.doi.org/10.1149/2.1181714jes>.
- [31] M. Safari, C. Delacourt, Aging of a commercial graphite/LiFePO₄ cell, *J. Electrochem. Soc.* 158 (2011) A1123–A1135, <http://dx.doi.org/10.1149/1.3614529>.
- [32] S. Käbitz, et al., Cycle and calendar life study of a graphite/LiNi₁/3Mn₁/3Co₁/3O₂ Li-ion high energy system. Part A: Full cell characterization, *J. Power Sources* (ISSN: 03787753) 239 (2013) 572–583, <http://dx.doi.org/10.1016/j.jpowsour.2013.03.045>.
- [33] B. Li, et al., A review of solid electrolyte interphase (SEI) and dendrite formation in lithium batteries, *Electrochem. Energy Rev.* (ISSN: 2520-8136) 6 (1) (2023) 7, <http://dx.doi.org/10.1007/s41918-022-00147-5>.
- [34] Y. Li, et al., Data-driven health estimation and lifetime prediction of lithium-ion batteries: A review, *Renew. Sustain. Energy Rev.* (ISSN: 18790690) 113 (2019) <http://dx.doi.org/10.1016/j.rser.2019.109254>.
- [35] A. Soto, A. Berrueta, M. Mateos, P. Sanchis, A. Ursua, Impact of micro-cycles on the lifetime of lithium-ion batteries: An experimental study, *J. Energy Storage* (ISSN: 2352-152X) 55 (2022) <http://dx.doi.org/10.1016/j.est.2022.105343>, [Online]. Available: <https://www.sciencedirect.com/science/article/pii/S2352152X2201338X>.
- [36] A. Marongiu, M. Roscher, D.U. Sauer, Influence of the vehicle-to-grid strategy on the aging behavior of lithium battery electric vehicles, *Appl. Energy* (ISSN: 03062619) 137 (2015) 899–912, <http://dx.doi.org/10.1016/j.apenergy.2014.06.063>.
- [37] M. Petit, E. Prada, V. Sauvart-Moynot, Development of an empirical aging model for Li-ion batteries and application to assess the impact of vehicle-to-grid strategies on battery lifetime, *Appl. Energy* (ISSN: 0306-2619) 172 (2016) 398–407, <http://dx.doi.org/10.1016/j.apenergy.2016.03.119>, [Online]. Available: <https://www.sciencedirect.com/science/article/pii/S0306261916304500>.
- [38] A. Leippi, M. Fleschutz, M.D. Murphy, A review of EV battery utilization in demand response considering battery degradation in non-residential vehicle-to-grid scenarios, *Energies* (ISSN: 1996-1073) 15 (9) (2022) 3227, <http://dx.doi.org/10.3390/en15093227>, [Online]. Available: <https://www.mdpi.com/1996-1073/15/9/3227>.